

A novel $\text{AlCo}_{1.2}\text{Cr}_{0.8}\text{FeNi}_{2.1}$ eutectic high entropy alloy with excellent corrosion resistance

Yujing Yang ^a, Yong Dong ^{a,*}, Shichao Liu ^b, Shougang Duan ^{a,c,**}, Chuanqiang Li ^a, Peng Zhang ^a

^a School of Materials and Energy, Guangdong University of Technology, Guangzhou 510006, China

^b School of Iron and Steel, Soochow University, Suzhou 215021, China

^c School of Materials Science and Engineering, South China University of Technology, Guangzhou 510640, China

ARTICLE INFO

Keywords:
Eutectic high entropy alloys
Mechanical property
Corrosion behavior
Corrosion mechanism
Passive film

ABSTRACT

A novel $\text{AlCo}_{1.2}\text{Cr}_{0.8}\text{FeNi}_{2.1}$ eutectic high entropy alloy (EHEA) was designed and prepared. The microstructure of the as-cast alloy was characterized that a fine lamellar structure composed of FCC (L1_2) phase and B2 phase. The mechanical of the EHEA was studies by the tensile tests, and the corrosion properties of the EHEA in 3.5 wt% NaCl solution at room temperature was investigated. The results shown that the alloy exhibits synergistic effect of strength- plasticity with a high tensile strength of 1048.42 MPa and an excellent elongation of 18.92%. Potentiodynamic polarization test and electrochemical impedance spectroscopy (EIS) indicated that the EHEA exhibits spontaneous passivation in 3.5 wt% NaCl solution, forming a protective passive film that exhibits p-type and n-type semiconductor properties, with the main components of Al_2O_3 , CoO , Cr_2O_3 , Fe(OH)_3 , and NiO . Furthermore, the corrosion mechanism of EHEA was discussed.

1. Introduction

Recently, many scholars have shown great interest in the high entropy alloys (HEAs) because of its unique solid structure and excellent comprehensive properties. High entropy alloys and multi-principal components alloys were initially proposed by Yeh and Cantor in 2004 [1,2]. It initially referred to equi-atomic ratio alloys, but later gradually developed into non equi-atomic ratio alloys. Nowadays, it is generally accepted that alloys that consist mostly of five or more elements, with an element content ranging from 5% to 35%, are classified as high-entropy alloys. This alloy has four distinct properties: high entropy, slow diffusion, lattice distortion, and cocktail effect [3]. Early research mainly focused on single-phase solid solution high entropy alloys, such as CoCrFeMnNi with face-center cubic (FCC) structure [4], ZrNbTiVHF with body-center cubic (BCC) structure [5], and GdHoLaTbY with hexagonal close-packed structure [6]. Subsequently, to improve the comprehensive mechanical properties of HEAs, the HEAs with multi-phases structure were researched. For example, Lu et al. successfully prepared $\text{AlCoCrFeNi}_{2.1}$ eutectic high entropy alloy (EHEA) with FCC/B2 structure, achieving a balance between strength and plasticity [7]. Similarly, HEAs with BCC/B2 phases [8], FCC/Laves phases [9],

and BCC/Laves phases [10] have also been researched. However, HEAs will face various complex environments in industrial applications such as petrochemicals, aerospace, shipbuilding, etc, so lots of studies have been undertaken to combine the strength with other properties, including wear resistance [11], oxidation resistance [12], radiation damage resistance [13], and so on, to widen the service performance of HEAs. In addition, corrosion is one of the main forms of failure, so it is crucial to research the corrosion property and study the corrosion behavior and mechanism of HEAs.

Nevertheless, corrosion is a major cause of material failure. Therefore, investigating corrosion resistance and corrosion mechanisms of materials is critical for developing novel corrosion resistant materials. Because of the simple solid solution structure and capacity to hold many passivation components (such as Cr, Ni, Mo, etc.), HEAs have better corrosion resistance than traditional alloys such as Ni-based alloys and stainless steel, making it promising corrosion resistant materials [14]. The $\text{Hf}_{0.5}\text{Nb}_{0.5}\text{Ta}_{0.5}\text{Ti}_{1.5}\text{Zr}$ exhibits astonishing corrosion resistance better than 316 L SS in 3.5 wt% NaCl solution with a lower current density of $0.34 \mu\text{A}/\text{cm}^2$ and a higher pitting potential of +8.36 V [15]. Besides, the corrosion behavior of HEAs in different environments has been studied. Wan et al. [16] investigated the corrosion behavior and

* Corresponding author.

** Corresponding author at: School of Materials and Energy, Guangdong University of Technology, Guangzhou 510006, China.

E-mail addresses: dongyong5205@163.com (Y. Dong), sgduan0410@163.com (S. Duan).

passive film performance of as-cast Co-free $\text{Al}_{0.8}\text{CrFeNi}_{2.2}$ EMEA in several environments (0.5 M NaCl, 0.5 M Na_2SO_4 , 0.5 M H_2SO_4 , and 0.5 M HCl). The findings show that the dual-phase eutectic heterogeneous structure is the root cause of the BCC phase's preferential corrosion in all corrosive environments. Shi et al. [17] researched the influence of Al content on the corrosion resistance of $\text{Al}_x\text{CoCrFeNi}$ ($x=0.3, 0.5$, and 0.7), and found that as the Al concentration in HEA increased, the corrosion resistance decreased due to the presence of the BCC phase. However, the $\text{AlCoCrFeNi}_{2.1}$ EHEA has both high tensile strength (~900 MPa) and high plasticity (elongation is reached ~25%), exhibits similar corrosion resistance to $\text{Al}_x\text{CoCrFeNi}$ ($x=0.3, 0.5, 0.7$) [7, 17,18].

The $\text{AlCoCrFeNi}_{2.1}$ EHEA have gotten a lot of attention since its announcement in 2014 because of its remarkable castability and excellent mechanical properties, which have the potential for industrial applications. Wei and Qin [19] reported the corrosion performance of the $\text{AlCoCrFeNi}_{2.1}$ EHEA in sulfuric acid solution, revealing that the passive performance of the alloy is close to that of 304 stainless steel. Generally, adding Cr element to the alloy can form a Cr_2O_3 oxide film on the alloy surface, giving it good oxidation and corrosion resistance. However, there are Cr-rich BCC precipitates in the B2 phase of the as-cast $\text{AlCoCrFeNi}_{2.1}$ EHEA, indicating that Cr element segregation phenomenon. Commonly, precipitates are thought to increase strength but decrease corrosion resistance of alloys because of the galvanic corrosion. For example, Han et al. [20] reported that the segregation of alloying elements shows a negative impact on the corrosion behavior of ultra-fine grained Cantor alloy. Besides, Chai et al. [21] found that $\text{FeCoNiCr}0.5$ MPEA shows an outstanding anticorrosion performance in 3.5% NaCl solutions, while the excess Cr addition leads to the noticeable localized corrosion, Cr-induced segregation significantly deteriorates the corrosion resistance in the quaternary FeCoNiCr MPEA.

In this work, replacing a certain amount of Cr with Co element to avoid the appearance of Cr-rich BCC precipitates in the $\text{AlCo}_{1.2}\text{Cr}_{0.8}\text{-FeNi}_{2.1}$ alloy, and research its microstructure by X-ray diffraction (XRD), scanning electron microscope (SEM), and transmission electron microscopy (TEM). Tested its tensile property at room temperature, electrochemical performance in 3.5 wt% NaCl solution. Utilizing the electrochemical impedance spectroscopy (EIS) and Mott-Schottky test to evaluated the performance of the passive film formed in 3.5 wt% NaCl solution, and the chemical composition and elements state of the passive film was determined by X-ray photoelectron spectroscopy (XPS). And the surface potential difference of the dual-phases was measured by Scanning Kelvin Probe Force Microscopy (SKPFM). Finally, the microstructure, mechanical property, corrosion performance and mechanism were discussed based on the characterization results.

2. Experiment

2.1. Material prepare and microstructure characterization

The cylindrical ingot of $\text{AlCo}_{1.2}\text{Cr}_{0.8}\text{FeNi}_{2.1}$ (at%) alloy (denoted as EHEA in the following paragraph) with a diameter of 30 mm and a height of 170 mm was prepared by vacuum medium frequency induction melting. The raw materials used are high-purity aluminum, cobalt, and nickel in 99.9 wt%, chromium and iron in 99.5–99.6 wt%.

Wire electrical discharge machining (WEDM) was used to cut the test samples from the cylindrical ingot. Phase identification of the EHEA was carried out by X-ray diffraction (XRD, Bruker D8 Advance with Cu radiation target) at 40 kV and 40 mA with the 2 θ scanning range of 20–100 degrees, and diffraction rate of 6 deg/min. The microstructure and elements distribution of the EHEA was observed by optical microscope (OM, DMi8C, Leica) and scanning electron microscope (SEM, SU8010, Hitachi) with energy dispersive spectroscopy (EDS) after etched with diluted aqua regia solution. Besides, the nano-precipitated phase and nano-scale phase interface of the material were characterized by transmission electron microscopy (TEM, Talos F200S, FEI). The samples for

TEM were prepared by mechanical grinding and twin-jet electrolytic thinning (electrolyte: 92% ethanol + 8% perchloric acid, in vol%).

The surface Volta potential difference between dual-phases of EHEA were measured by Atomic Force Microscope (AFM, Dimension FastScan, Bruker) using Scanning Kelvin Probe Force Microscopy (SKPFM, Multimode 3D, Bruker Corporation). In the measurements, a magnetic etched silicon probe (MESP) ($k = 2.8 \text{ N/m}$, Bruker Corporation, CA) was employed. Before the experiment, calibrate the tip with a gold reference sample. Finally, NanoScope Analysis software was used to analyze the results.

2.2. Mechanical properties tests

The tensile samples with a gauge length of 20 mm were cut from the ingot by WEDM. The tensile test was conducted on universal testing machine (AGS-X Plus 100 kN, Shimadzu) with an initial strain rate of $1.0 \times 10^{-3} \text{ s}^{-1}$ at ambient temperature. To make sure the data was reliable, the test was performed at least three times.

2.3. Electrochemical tests

Electrochemical tests were carried out using a CORRTEST electrochemical workstation in a typical three-electrode system with a saturated calomel electrode (SCE) as reference electrode (RE), a platinum sheet as counter electrode (CE), an EHEA sample (the exposure area is 1 cm^2) as work electrode (WE). Before testing, a constant potential polarization at a potential of -0.2 V (vs. OCP) for 5 minutes was performed to remove the oxide film on the alloy surface. Then, the open-circuit potential (OCP) test was conducted for 1800 s to obtain a stable potential. Electrochemical impedance spectroscopy (EIS) was tested at OCP, with a frequency range of 10 kHz–10mHz and an alternating current (AC) of 10 mV. Finally, the potentiodynamic polarization test was carried out, with a scan rate of 1 mV/s and a voltage range of -0.2 V (vs. OCP) to 1 V (vs. OCP). The scan stops when the current density exceeds 1 mA/cm^2 . The electrolyte used in the tests was 3.5 wt% NaCl solution, in which each sample was tested at least three times.

The Mott-Schottky test with a frequency of 1 kHz using an AC of 10 mV and a fast-scanning rate of 50 mV/s from -1 V to 1 V (vs. SCE) was conducted to evaluate the semiconductor properties of passive film on the EHEA surface in 3.5 wt% NaCl solution. Before the test, the sample was polarized at a constant potential of -0.2 V (vs. OCP) for 300 s in order to remove the surface oxide film. It was then polarized at a constant potential of 0 V (vs. SCE) for 3600 s in order to establish a stable surface passive film.

2.4. XPS analysis

After obtaining a stable passive film through the above constant potential polarization, the chemical composition of the passive film was determined by X-ray photoelectron Spectroscopy (XPS, Escalab 250Xi, Thermo Fisher Scientific) with monochromatic Al-K α source. The X-ray spot is 650 μm in diameter, with a voltage of 15 kV and a current of 15 mA. XPS data was analyzed by the software Avantage, and standard carbon C1s binding energy (284.8 eV) was used to calibrate.

3. Results and discussion

3.1. Microstructure and phase identification of the EHEA

The XRD, OM, SEM and EDS results shown in Fig. 1. The XRD results in Fig. 1(a) show that the EHEA is composed of FCC phase and BCC (B2) phase. The strongest peaks of FCC and BCC (B2) phase are (111) and (110) peaks, respectively, and the corresponding volume fraction are 61.0% and 39.0%. According to the Bragg equation, the lattice constants of the FCC and BCC (B2) phases can be calculated was 3.583 Å and 2.875 Å, respectively. The microstructure of the EHEA is a typical dual-

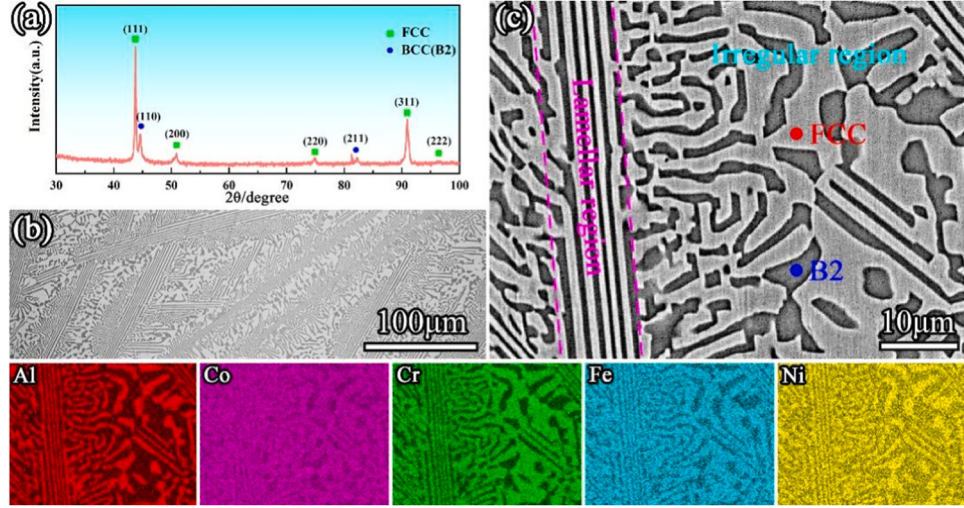


Fig. 1. Microstructure and composition of EHEA. (a) XRD pattern; (b) Optical microscope image; (c) BSE-SEM image and EDS mapping showing the elemental distribution.

phase eutectic structure consisting of long and straight lamellar and irregular structures, as seen by the OM image in Fig. 1(b). The content of the FCC and BCC (B2) phases was measured using Image software through multiple low magnification metallographic images at different positions in samples, with values of 59.64% and 40.36% respectively, which is not significantly different from the results calculated by the previous XRD. Fig. 1(c) shows the high magnification BSE-SEM, revealing that the microstructure can be split into lamellar and irregular regions. Combined with the results of elemental distribution, the light gray regions marked by red dot are rich in Co, Cr, and Fe but poor in Al and Ni elements, indicating FCC phases. The dark gray regions

marked by blue dot are exactly the opposite, indicating the ordered BCC (B2) phases, which is similar to the previously reported HEAs [19,22].

Further characteristics by TEM was displayed in Fig. 2. The select area electron-diffraction (SAED) patterns show the existence of super-lattice point revealing the ordered structure of FCC and BCC phase, namely L₁ and B2 phase. It can be observed from the dark-field (DF) and high-resolution transmission electron microscopy (HR-TEM) of FCC phase that there are lots of nano-precipitates with an average size of 2.5 ± 0.8 nm dispersed within the FCC phase, the SAED obtained from fast Fourier transform (FFT) is confirming that the nano-precipitates (NPs) are L₁ phases and the matrix phase is FCC phase. Fig. 2(c1) shows the

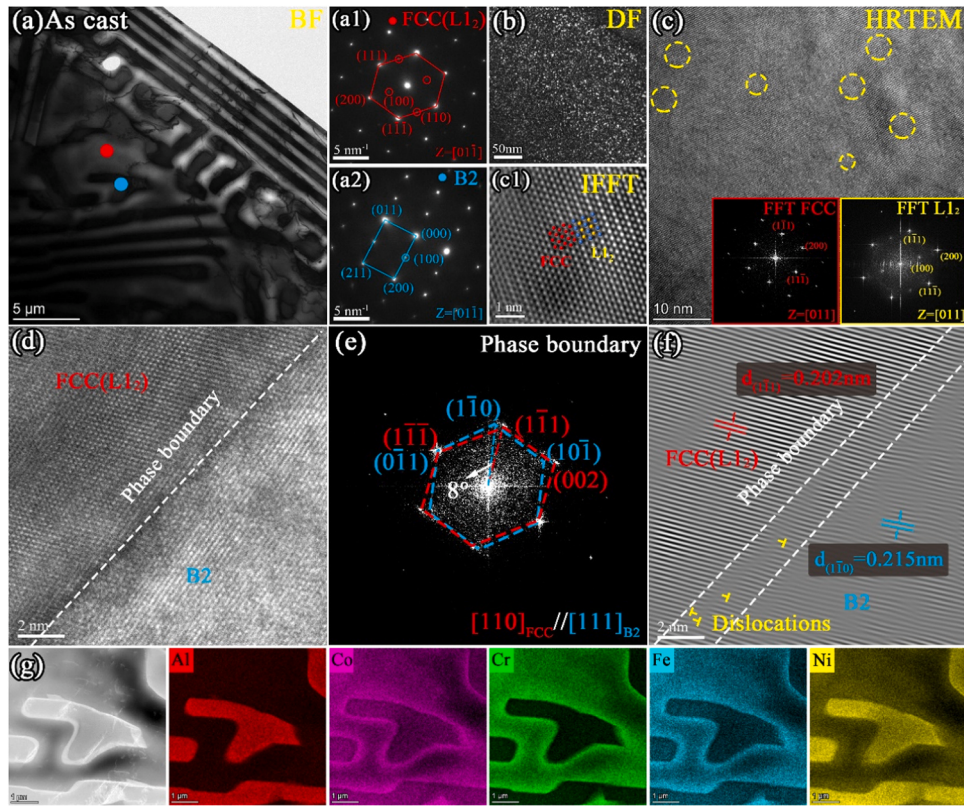


Fig. 2. TEM images of the EHEA. (a) BF-TEM image; (a1-a2) SAED patterns of FCC(L1₂) and B2 phase; (b) DF-TEM image of FCC phase region; (c) HR-TEM of FCC phase region; (c1) IFFT of FCC phase and L₁₂ nano-precipitate; (d) HR-TEM of the FCC(L₁₂) and B2 phases; (e) FFT and (f) IFFT images of (d); (g) EDS-TEM Mapping.

lattice arrangement of L1₂ and FCC obtained through inverse fast Fourier transform (IFFT), indicating that the interface relationship between L1₂ and FCC is completely coherent. HRTEM of the phase boundary of FCC and B2 phases is displayed in Fig. 2(d), and the SAED obtained through FFT from the HRTEM is shown in the Fig. 2(e), indicating the [110] and [111] crystal zone axis phase of the FCC and B2 phases. It can be observed that the (111) crystal plane of the FCC phase is parallel to the (110) crystal plane of the B2 phase, confirming the orientation relationship between the two phases is [110]_{FCC}//[111]_{B2}, which is the classical Kurdjumov-Sachs (KS) relationship. Fig. 2(f) shows the corresponding lattice fringes obtained from the inverse Fourier transform of the g(1–11) and g(1–10) diffraction points of FCC and B2 phases, demonstrating a semi-coherent relationship accompanied by some dislocations and lattice mismatches. The Mapping in Fig. 2(g) by EDS-TEM also proves the results in previous EDS of SEM. And the elements content of different phases was listed in Table 1.

3.2. Mechanical properties

The tensile stress-strain curves and strain hardening rate curve of the EHEA are illustrated in Fig. 3. And the yield strength ($\epsilon_{0.2}$), engineering / true stress (σ / σ_T), and engineering / true strain (ϵ / ϵ_T) are listed in Table 2. The EHEA exhibits both high strength (tensile strength: 1048.42 MPa) and good plasticity (elongation: 18.92%), and the difference of yield strength and tensile strength reaches \sim 572 MPa, signifying that the EHEA has excellent work hardening ability, which is a reason for the EHEA has a high yield strength and large elongation simultaneously. Compared to AlCoCrFeNi_{2.1} [23], the strength slightly decreases while the plasticity increases, which may be due to the increase in the content of FCC phase in the alloy caused by Co replacing Cr element, and the absence of BCC precipitation strengthening phase in B2 phase. The strain-hardening rate ($\theta = d_{\sigma T} / d_{\epsilon T}$) was obtained from the true stress-strain curve, as illustrated in Fig. 3(b), which is commonly separated into three stages [24]. The strain hardening rate decreases sharply in the first (ϵ_T less than 2.5%) and third (ϵ_T larger than 17.3%) stages which is related to the elastic deformation and plastic deformation have reached its limits, while it decreases gradually in the second stage (with the ϵ_T range of 2.5–17.3%).

Fig. 4 shows the tensile surface and fracture morphology of the EHEA. It can be observed from Fig. 4(a) that there are a few slip lines in the FCC phase, while cracks appear in the hard-B2 phase. Cracks may expand along the phase boundary or directly through the B2 phase in the direction of the vertical stress. Fig. 4(b-d) display that the feature of the fracture is trench like shapes on the lamellar regions and dimples on the irregular regions. The formation of both fracture characteristics is related to the combination of ductile fracture of FCC phase and brittle fracture of B2 phase: the FCC phases occur plastic deformation and thinning to bright lines under stress, while the B2 phases hardly deform and remain at the bottom with fan-shape patterns.

3.3. Corrosion resistance analysis

3.3.1. Potentiodynamic polarization test

Fig. 5 displays the potentiodynamic polarization curve of the EHEA at room temperature in a 3.5 wt% NaCl solution. The anodic

polarization region can be divided into three regions of active dissolution region, self-passive region, and trans-passive region. The significant self-passive region indicating that the EHEA can spontaneously passivate in 3.5 wt% NaCl solution [25]. According to Tafel extrapolation, the polarization curve can be used to calculate the corrosion potential (E_{corr}) and the self-corrosion current density (I_{corr}), which are -0.278 V (vs. SCE) and 1.528E-7 A/cm², respectively. Besides, the breakdown potential (E_{pit}) and passivation current density (I_{pass}) can also be obtained from the potentiodynamic polarization curve, which are 0.148 V and 3.348E-6 A/cm², respectively. And ΔE (E_{pit} - E_{corr}) represents the passivation region, which was calculated as 0.426 V. Moreover, it can be discovered that there are some current fluctuations in the passive region, especially when approaching the E_{pit} , indicating the generation of metastable pitting corrosion and gradually developing into steady-state pitting, ultimately leading to the rupture of the passivation film [17]. The corrosion morphologies at different potentials (E_{OCP} , 0 V, E_{pit}) during the polarization test in the Fig. 6 are used to understand the formation process of pitting corrosion. As can be seen, the EHEA has not begun to be corrode at the potential of E_{OCP} , but the B2 phase in the dashed circle turns black starting from the FCC / B2 phase boundary under the current increasing. Afterwards, the B2 phase near the phase boundary begins to dissolve at the potential of 0 V, forming pitting corrosion. It can be observed that Al and Ni elements have been lost from the corresponding element Mapping in Fig. 6(b). Subsequently, the pitting corrosion gradually developed and the corrosion area expanded, forming a selective dissolution of B2 phase (as indicated by the blue arrow), leaving behind a network of FCC phases rich in CoCrFe elements. Interestingly, the pitting corrosion seems to nucleate preferentially in the irregular regions rather than the lamellar regions. The phenomenon of preferential corrosion in B2 phase is selective corrosion, which can be related to the micro-galvanic corrosion due to the potential difference between the FCC phase and B2 phase [26]. It will be analyzed in detail by SKPFM subsequently.

3.3.2. EIS measurement

Electrochemical Impedance Spectroscopy (EIS) test was performed to characterize the electrochemical corrosion behavior of the as cast EHEA. The Nyquist curve in Fig. 7(a) is a semi-circular arc with the center below the X-axis. The phenomenon is indicating uneven interface charge transfer and spontaneous passivity of corrosion, according to the report previous [27]. Generally, the larger the radius of the capacitor arc, the greater the polarization resistance, and the better its ability to block current, exhibiting better corrosion resistance performance. The Bode shown in Fig. 7(b) indicates that the impedance modulus increases with the decrease of frequency, reaching 10^5 Ohm*cm², while the phase angle increases and then decreases. The highest phase angle in the bode diagram is around -80 degrees in a wide frequency region (10^0 – 10^2 Hz), indicating the passive film of EHEA has relatively high protective properties [28].

Afterwards, select the electrochemical equivalent circuit (EEC) illustrated in the inset of Fig. 7(a) and use Zview software to fit the EIS data to further analyze the impedance characteristics of the EHEA. In the EEC model, two constant phase angle elements (CPE) are used to compensate for the non-uniformity of the corrosion interface [29]. The two CPEs represent the capacitance of passive film and the electrochemical response of the double layer, marked as CPE₁ and CPE₂, and the electrical impedance of CPE can be calculated by formula (1) [30].

$$Z_{CPE} = \frac{1}{Y_0(\omega j)^n} \quad (1)$$

Where Y_0 represents a proportionality constant, ω is angular frequency, j signifies the imaginary unit, and n is fitted exponential with the range of 0–1. When $n=0$, CPE represents pure resistance, when $n=0.5$, it serves as Warburg impedance, and when $n=1$, it represents ideal capacitance.

Table 1

Chemical composition of FCC and B2 phases in different regions of the EHEA by TEM-EDS (at%).

Alloy	Regions	Element (at%)				
		Al	Co	Cr	Fe	Ni
EHEA	Lamellar-FCC	7.94	22.06	18.66	20.36	30.98
	Lamellar-B2	27.78	13.97	4.08	11.30	42.87
	Irregular-FCC	8.94	20.82	18.41	19.72	32.11
	Irregular-B2	26.69	15.76	6.23	10.71	40.61

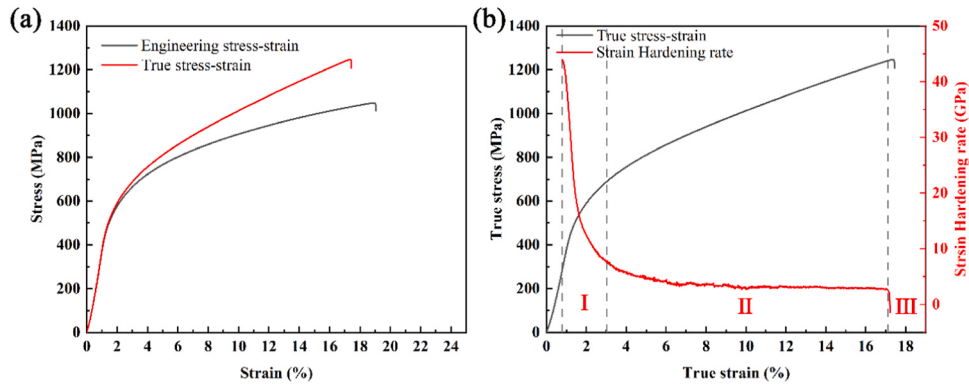


Fig. 3. Tensile stress-strain curves (a) and strain hardening rate curve (b) of the EHEA.

Table 2
Tensile test results of the EHEA.

Alloys	$\sigma_{0.2}$ (MPa)	σ (MPa)	ε (%)	σ_T (MPa)	ε_T (%)
EHEA	476.8	1048.6	18.9	1246.7	17.4
	± 23.2	± 2.7	± 1.4	± 18.5	± 1.2
Ni _{2.1}	561.87	1068.54	17.84	-	-
[23]					

Besides, the three resistors signify the solution resistance (R_s), passive film resistance (R_1), and charge transfer resistance (R_2), respectively. Moreover, the sum of R_1 and R_2 can be used to represent the polarization resistance (R_p) [31]. As displayed in Fig. 7, the solid line representing the fitted data coincides well with the dotted line of the experimental data, which proves that the EEC is appropriate. The chi square value (χ^2) as a specific indicator of fitting quality and other fitting parameters are listed in Table 2.

The effective capacitance of CPE can be calculated using formula (2) proposed by Hirschorn et al. [32]:

$$C_{\text{eff}} = Y_0^n R_{ct}^{-n} \quad (2)$$

Where Y_0 and R_{ct} refer to CPE₁ and R_1 . Subsequently, we can calculate the thickness of the passivation film of the EHEA by the formula following [33]:

$$d_{\text{eff}} = \frac{\epsilon \epsilon_0}{C_{\text{eff}}} \quad (3)$$

Where ϵ_0 is the permittivity of vacuum, the value is 8.8542×10^{-14} F/cm, the ϵ relative dielectric constant taken as 15.6, which is suitable for HEAs [34].

In summary, in the fitting results of EIS, the value of n represents the type of CPE. When $n_1 = 0.93$, the CPE₁ severs capacitance, while $n_2 = 0.54$, and CPE₂ is closer to Warburg impedance, indicating that the passive film is inhomogeneous [30]. The R_p commonly utilized to represent the corrosion resistance of alloy [35], while the EHEA has a high value of $R_p = 1.96 \times 10^5 \Omega \cdot \text{cm}^2$ revealing an excellent corrosion resistance. Additionally, the thickness of the passive film of the EHEA

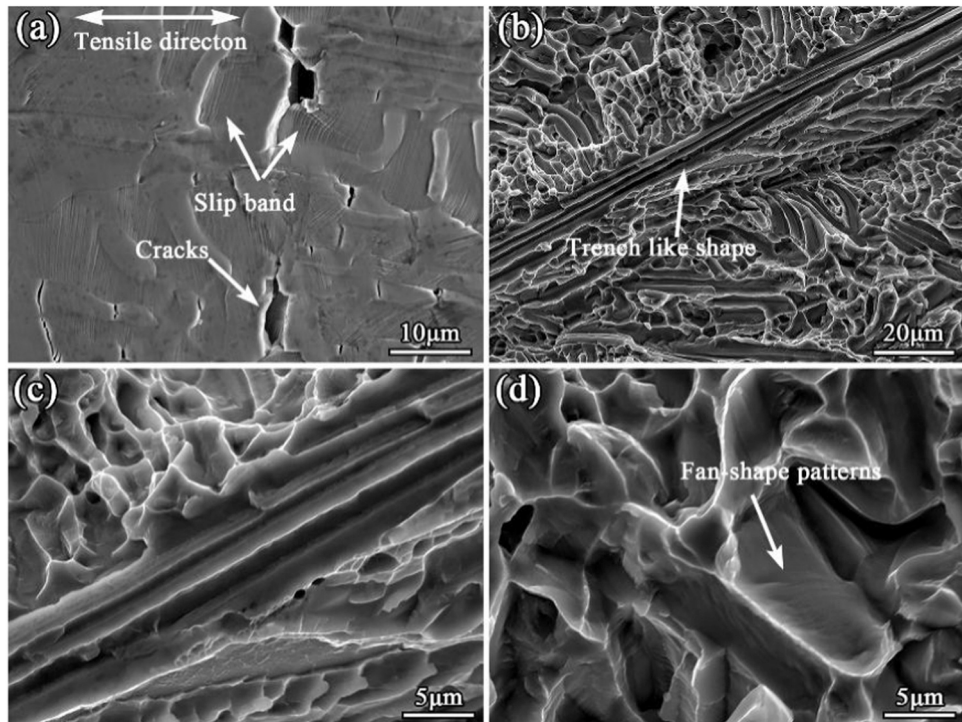


Fig. 4. Tensile surface and fracture morphology of the EHEA. (a) Surface morphology, (b) low magnification fracture morphology, (c-d) high magnification fracture morphology in lamellar and irregular region.

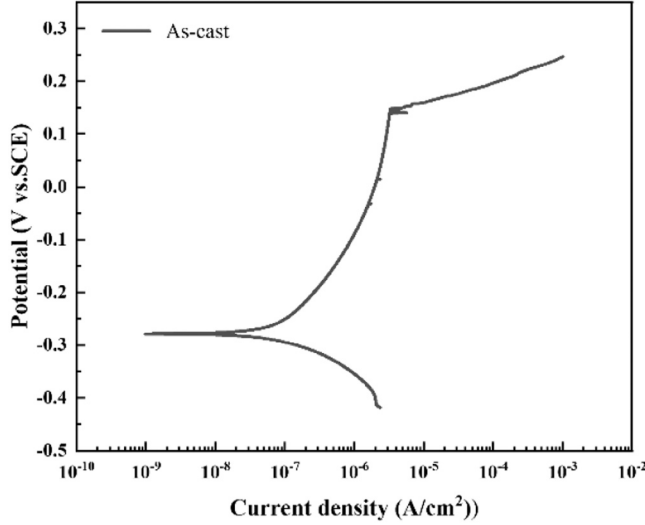


Fig. 5. The potentiodynamic polarization curve of the EHEA in 3.5 wt% NaCl solution.

was calculated by formula (3), which is 0.64 nm. Mott-Schottky test were investigated to further characterize the defects and semiconductor properties of the passive film.

3.3.3. Research of the passive film

The M-S plot can reveal the relationship of the electrochemical capacitance at the interface between the passive film and electrolyte and the applied potential. Based on the slope of this change, the semiconductor types of the passivation film can be defined, i.e., p-type semiconductor with negative slope and n-type semiconductor with positive slope. Based on the Mott-Schottky theory, the relationship be-

tween the space charge capacitance and voltage of semiconductors can be represented as follows [36]:

$$\frac{1}{C^2} = \pm \frac{2}{\varepsilon \epsilon_0 e N} (E - E_{FB} - \frac{kT}{e}) \quad (4)$$

In the equation, C signifies the capacitance of the space charge region, ε and ϵ_0 has been mentioned in Section 3.3.2, e is the electron charge (1.602×10^{-19} C), N represents carrier density of semiconductor, N_A was signed when it is p-type, N_D was signed when it is n-type; E_{FB} denotes the flat band potential, K is the Boltzmann constant (1.381×10^{-23} J/K), and T remains the absolute temperature (K), respectively.

The M-S curves of the EHEA after passivation at 0 V (vs.SCE) for 3600 s is display in Fig. 8. The passive film exhibits p-type semiconductor in the range of -1 V to -0.6 V, transforms into n-type semiconductor in the range of -0.6 V to 0.25 V, and then transforms back into p-type semiconductor after 0.25 V. The main carriers of p-type semiconductors in the first region (-1 V ~ -0.6 V) are cation vacancies as acceptor states, such as Cr_2O_3 , FeO , NiO , the second region (-0.6 V ~ 0.25 V) are oxygen holes or cation interstitials as donor states, such as Al_2O_3 , CoO , Co_2O_3 , Fe_2O_3 , FeOOH [37]. The increase in capacitance value in the third region can be attributed to the increase in hole concentration in the valence band, which is not directly related to semiconductor properties [38]. The acceptor density (N_A) and donor densities (N_D) was calculated by formula (4) and listed in Table 3. The magnitude of N_A and N_D is reaching to 10^{20} - 10^{21} , which is similar to the stainless steel, indicating that the EHEA has a corrosion resistance similar to common stainless steel [39,40].

The elements composition and valence state of the passive film were determined by XPS. The survey spectrum, the high-resolution detailed spectra of $\text{Al } 2p3/2$, $\text{Co } 2p3/2$, $\text{Cr } 2p3/2$, $\text{Fe } 2p3/2$, $\text{Ni } 2p3/2$, $\text{O } 1s$ and the ionic fractions of different elements were shown in Fig. 9. The survey spectrum in Fig. 9(a) reveals the presence of Al, Co, Cr, Fe, Ni, C and O elements on the passive film of EHEA. The presence of C element may be

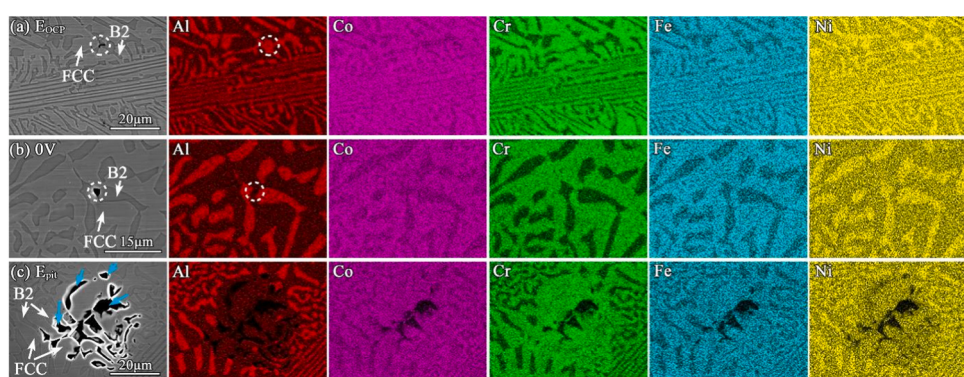


Fig. 6. The corrosion morphologies and Mapping by SEM at different potentials during the polarization test (ex-situ). (a) E_{OCP} ; (b) 0 V; (c) E_{pit} .

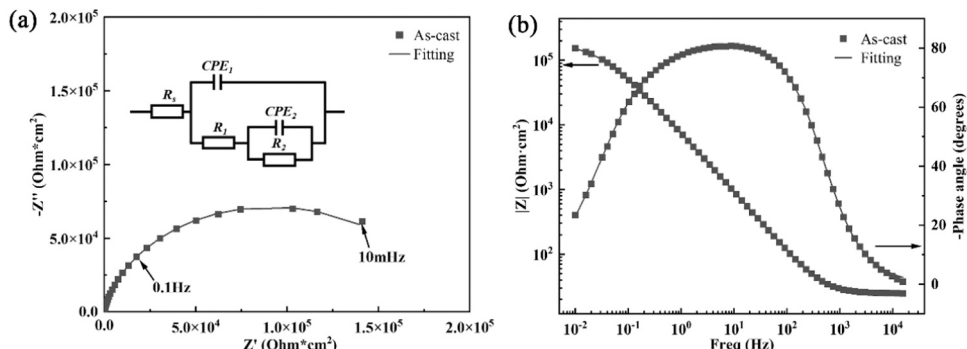


Fig. 7. The Nyquist (a) and Bode (b) curves of the EHEA in 3.5 wt% NaCl solution; the inset in (a) is EEC.

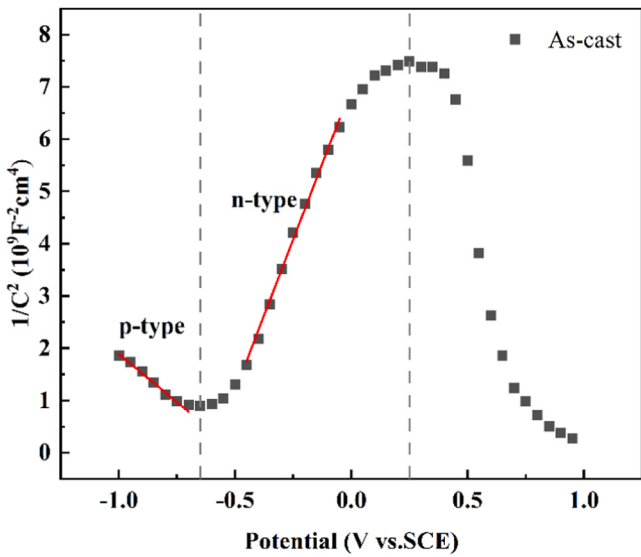


Fig. 8. Mott-Schottky curves of the EHEA after passivation at 0 V (vs.SCE) for 3600 s in 3.5 wt% NaCl solution.

Table 3

Electrochemical parameters of the EHEA of polarization tests in 3.5 wt% NaCl solution.

Alloy	E_{corr} (V)	I_{corr} (A/cm ²)	E_{pit} (V)	I_{pass} (A/cm ²)	ΔE (V)
EHEA	-0.278 ±0.013	(1.528 ±0.482) E-7	0.148 ±0.021	(3.348 ±0.379) E-6	0.426 ±0.033

accidental carbon pollution, while the presence of O element indicates the presence of metal oxides or hydroxides. As display in Fig. 9(b), Al element has two peaks of Al metal (72.7 eV) and Al^{3+}_{ox} oxide (74.4 eV) which is Al_2O_3 with little difference in content. The compactness of Al_2O_3 is poorer than that of Cr_2O_3 , which contributes less to the protection of passive film [41,42]. The spectra of Co shown in Fig. 9(c) can be divided to four peaks, i.e., Co metal (778.6 eV), Co^{2+}_{ox} (779.0 eV), Co^{3+}_{ox} (782.2 eV), Co^{2+}_{hy} (784.8 eV) and Co^{2+}_{sat} (787.2 eV). The peak of

Co^{2+}_{ox} represents CoO rather than Co_3O_4 , due to the presence of the peak of Co^{2+}_{sat} [43], the Co^{3+}_{ox} referring to Co_2O_3 , and the Co^{2+}_{hy} relating to $Co(OH)_2$. Among them, the content of CoO is highest, furthermore, CoO and $Co(OH)_2$ can decrease the diffusion rate of corrosive ions to improve the protective properties of passive film [44,45]. Whereupon, three peaks can be found in the spectra of Cr 2p3/2, which are Cr metal (574.3 eV), Cr^{3+}_{ox} (576.0 eV), and Cr^{3+}_{hy} (577.9 eV), indicating Cr_2O_3 and $Cr(OH)_3$, respectively. Since Cr_2O_3 in the passive film has an excellent density and thermodynamic stability, it is typically thought to be the primary cause of the great corrosion resistance [46–49]. And the spectra of Fe element are composed of Fe metal (707.2 eV), Fe^{2+}_{ox} (708.0 eV), Fe^{3+}_{ox} (710.3 eV), Fe^{3+}_{hy} (712.8 eV), and Fe^{2+}_{sat} (714.9 eV), revealing the presence of FeO , Fe_2O_3 or Fe_3O_4 , and $Fe(OH)_3$ or $FeOOH$ in the passive film. It is well known that the compactness of hydroxide is lower than that of oxide; hence, the high ratio of hydroxide / oxide in the Fe element reduces the compactness of passive film. Additionally, the Ni 2p3/2 spectra display four peaks as Ni metal (853.3 eV), Ni^{2+}_{ox} (853.8 eV), Ni^{2+}_{hy} (857.2 eV), and Ni^{2+}_{sat} (859.8 eV), relating to NiO and $Ni(OH)_2$. The metallic Ni has highest content due to its stability. The three peaks in Fig. 9(g) can be determined as O^{2-} (530.5 eV), OH^- (531.7 eV), and H_2O (533.0 eV), corresponding to metal oxides, metal hydroxides, and bound water in the passive film, respectively [50]. According to the previous researches [51,52], the bound water can assist capture metal ions to develop the passive film (Table 4).

Combined with the above results of TEM-EDS, it is can be inferred that the passive film on the FCC phase is mainly composed of the oxide / hydroxide of Co, Cr, Fe, and Ni elements, whereas the passive film on the B2 phase is primarily composed of the oxide / hydroxide of Al and Ni elements (Table 5).

3.3.4. SKPFM analysis

The Volta potential maps in different regions of the EHEA are display in Fig. 10. The relationship of Volta potential (V_{Volta}) and work function (WF) can be expressed by the formula as following [53]:

$$V_{Volta} = \frac{WF_{tip} - WF_{sample}}{-e} \quad (5)$$

Where the WF_{tip} and WF_{sample} refer to the work function of tip and EHEA, e is electron charge. According to the formula (5), a lower Volta

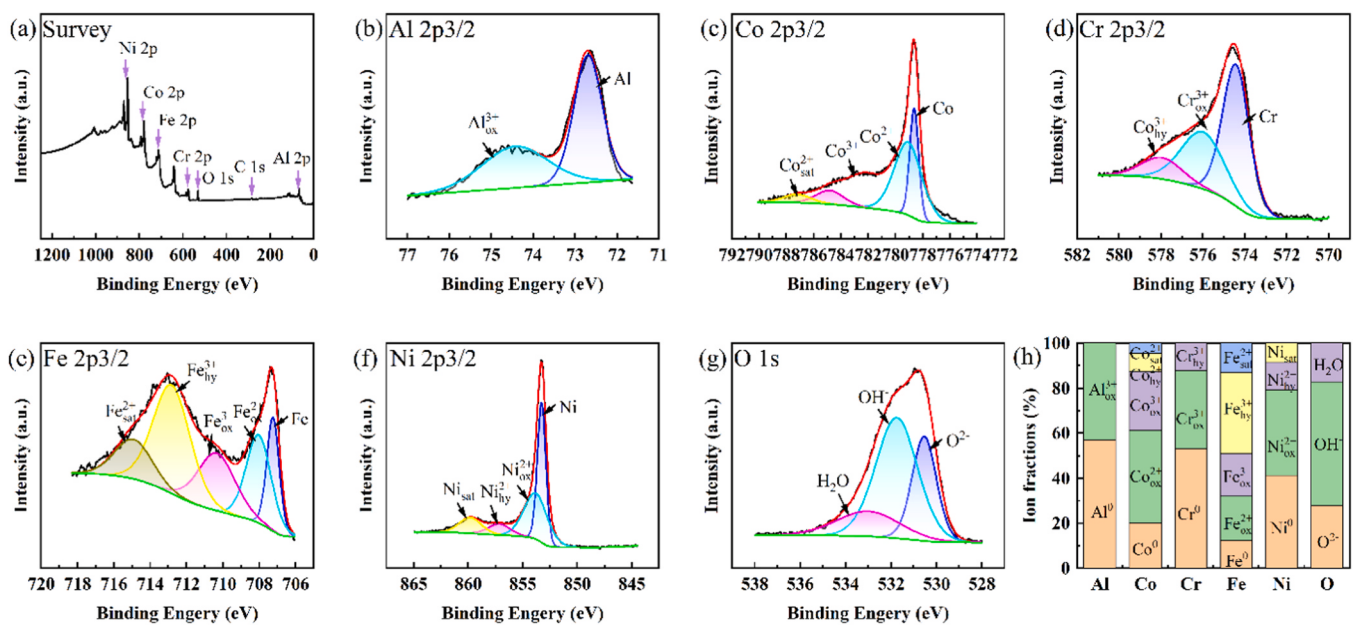


Fig. 9. XPS results of the passive film formed on the EHEA after passivation at 0 V (vs. SCE) for 3600 s in 3.5 wt% NaCl solution. (a) the survey spectrum, the high-resolution detailed spectra of (b) Al 2p3/2, (c) Co 2p3/2, (d) Cr 2p3/2, (e) Fe 2p3/2, (f) Ni 2p3/2, (g) O 1 s, (h) the ionic fractions of different elements.

Table 4

The fitting results of EIS of the EHEA in 3.5 wt% NaCl solution.

Alloys	R_s $\Omega \cdot \text{cm}^2$	CPE_1 $\times 10^{-5} \Omega^{-1} \cdot \text{cm}^{-2} \cdot \text{s}^n$	n_1	R_1 $\times 10^4 \Omega \cdot \text{cm}^2$	CPE_2 $\times 10^{-6} \Omega^{-1} \cdot \text{cm}^{-2} \cdot \text{s}^n$	n_2	R_2 $\times 10^5 \Omega \cdot \text{cm}^2$	R_p $\times 10^5 \Omega \cdot \text{cm}^2$	C_{eff} $\times 10^{-5} \text{F} \cdot \text{cm}^{-2}$	d_{eff} nm	$\Sigma \chi^2$ $\times 10^{-4}$
EHEA	24.82 ± 0.23	2.28 ± 0.12	0.93 ± 0.01	1.98 ± 0.20	6.52 ± 0.28	0.54 ± 0.08	1.76 ± 0.25	1.96 ± 0.28	2.14 ± 0.04	0.64 ± 0.13	0.94

Table 5

The acceptor density (N_A), donator densities (N_D) and the flat band potential (E_{FB}) calculated from Mott-Schottky curves.

Alloy	$N_A (10^{21} \text{ cm}^{-3})$	$N_D (10^{20} \text{ cm}^{-3})$	E_{FB} (V vs.SCE)
EHEA	2.46 ± 0.08	7.80 ± 0.46	-0.602 ± 0.02

potential corresponds to a lower work function, which signify that surface electrons are more likely to escape [54]. In the Volta potential maps, the bright regions with higher potential are FCC phases, while the B2 phases in the darker regions have a lower potential. As displayed in the Fig. 10(a) and (b), the Volta potential difference of the dual phases in the lamellar region is ~ 15.75 mV, while the Volta potential difference in the irregular region reaches ~ 17.59 mV, which may be the reason why pitting corrosion occurs preferentially in irregular regions (The abnormal bright area in the middle of Fig. 10(b) may be a pollutant). The B2 phase has lower Volta potential represents higher corrosion activity commonly, and it will be preferentially corroded as an anode in galvanic corrosion composed of FCC phase and B2 phase, which is consistent with the above corrosion morphology.

3.3.5. Corrosion mechanism

Fig. 11 reveals the corrosion mechanism of the EHEA. As displayed in Fig. 11(a), a protective passive film developed on the surface of EHEA because of the self-passive behavior in 3.5 wt% NaCl solution, according to the potentiodynamic polarization curve in Fig. 5. The chemical composition (determined by XPS in Figs. 9 and 10) of the passive film is the oxides / hydroxides of Al, Co, Cr, Fe, and Ni elements, with the oxides / hydroxides of the Cr element playing a major protective role, while Al appears to reduce corrosion resistance. Besides, the compositional differences between the FCC phase and the B2 phase result in

different densities and protective abilities of their passivation films. The Al-rich passive film of the B2 phase is relatively loose and prone to adsorbing Cl^- ions [54], forming pitting corrosion, as shown in Fig. 11 (b). Significantly, the pitting preferentially nucleates in irregular regions, as can be observed from the corrosion morphologies in Fig. 6, which may be related to the potential difference in different regions [19]. Furthermore, the B2 phases have a lower Volta potential as anodes in the micro-galvanic between the FCC phase and the B2 phase, accelerating the rate of corrosion and resulting in selective corrosion (Fig. 11 (c)). With the dissolution of the B2 phases, the electrolyte will enter the corrosion pores, increasing the area of contact with the FCC phase that has not yet formed a passive film, and the FCC phase also begins to corrode.

4. Conclusion

In this work, the microstructure, tensile property, corrosion resistance and mechanism of the $\text{AlCo}_{1.2}\text{Cr}_{0.8}\text{FeNi}_{2.1}$ have been tested and analyzed. Several conclusions were drawn as follows:

1. The microstructure of the EHEA is composed of a fine lamellar structure of FCC phase and B2 phase alternating and irregular eutectic structure. And there are a mount of nanoscale L1_2 precipitates in the FCC phase, while there is no precipitate in the B2 phase.
2. The EHEA exhibits a high tensile strength of 1048.42 MPa and an excellent elongation of 18.92%. The synergistic effect of strength-plasticity is mainly attributed to the lamellar structure where soft FCC phase and hard B2 phase intersect. The incompatibility between FCC providing plasticity and B2 providing strength during

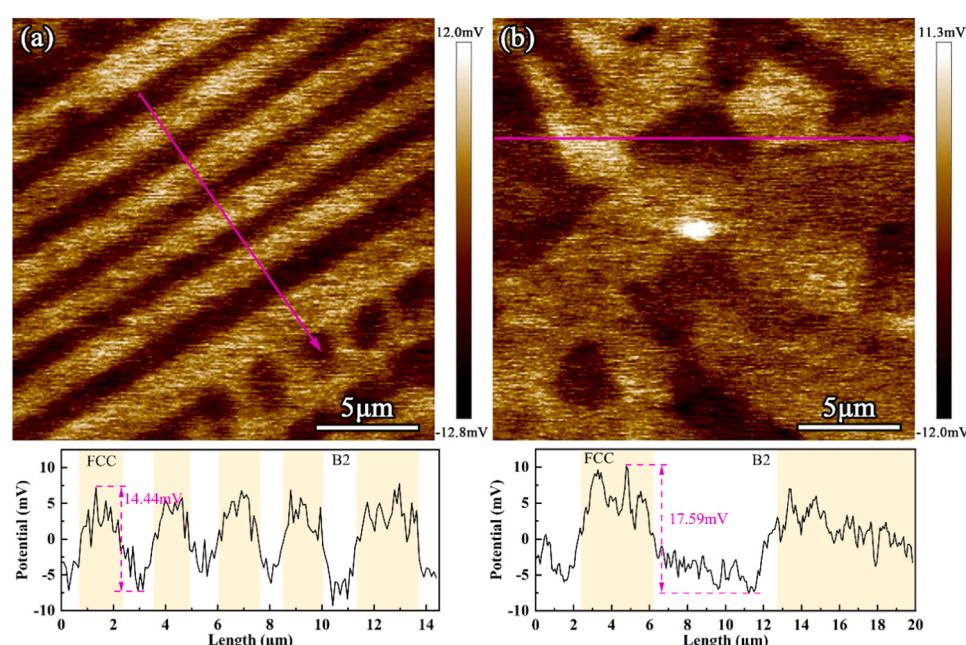


Fig. 10. The Volta potential maps and corresponding line profiles of the EHEA. (a) Lamellar region, (b) Irregular region.

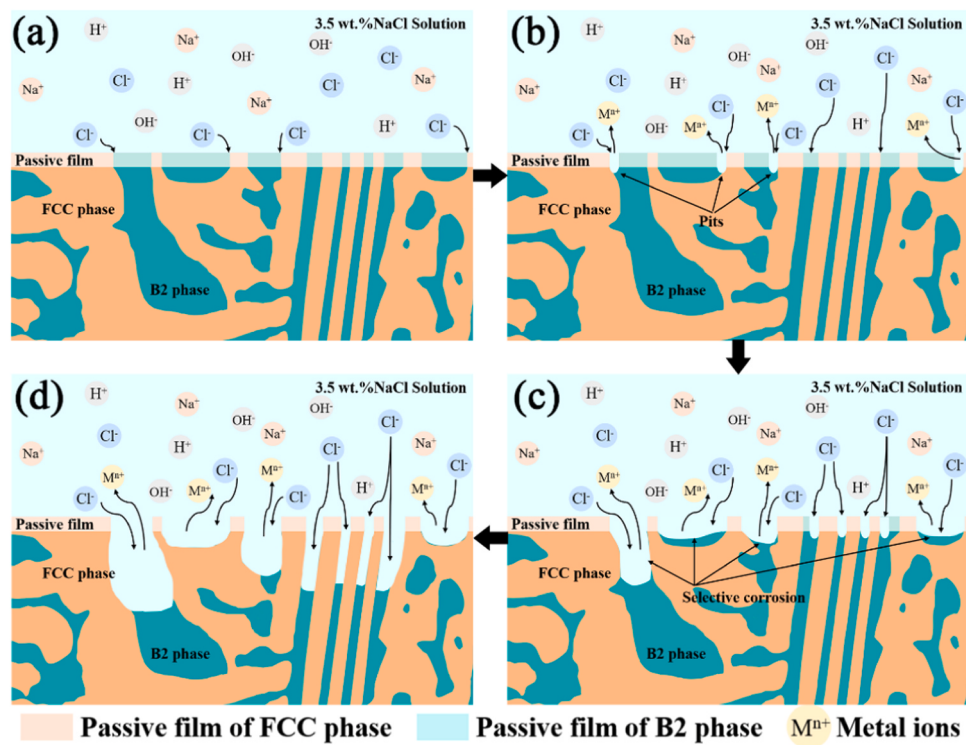


Fig. 11. The corrosion process of the EHEA in 3.5 wt% NaCl solution.

deformation leads to significant heterogeneous deformation strengthening.

3. The electrochemical results show that the EHEA has a high corrosion potential ($E_{corr} = -0.278$ V) and a low corrosion current ($I_{corr} = 1.528 \times 10^{-7}$ A/cm²), and the EIS results evaluated the performance of the passive film. The high polarization resistance ($R_p = 1.96 \times 10^5$ Ω·cm²) and the peak phase angle of ~80° indicates a better protective effect and stability.
4. The M-S test informed that the semiconductor properties of the passive film formed in 3.5 wt%NaCl solution at 0 V (vs SCE) are p-type and n-type semiconductors, with the value of N_A and N_D in the range of $10^{20} - 10^{21}$ cm⁻³, indicating a lower defect density that is easily attacked by Cl⁻ ions. Besides, the XPS results manifested the passive film is mainly composed of Al₂O₃, CoO, Cr₂O₃, Fe(OH)₃, and NiO.
5. The potential difference between the FCC phase and B2 phase in the irregular regions and lamellar regions of the EHEA is measured by SKPFM, and it is larger in the irregular regions. Hence, the pitting corrosion preferentially occurs in the irregular regions, consistent with the corrosion morphology at different potential. Subsequently, pitting corrosion gradually expanded, and the B2 phase in the layered area also began to corrode, forming a selective dissolution zone for the B2 phase. Then, the 3.5 wt% NaCl solution enters the corrosion pit and comes into contact with the FCC phase, and the FCC phase also begins to corrode.

CRediT authorship contribution statement

Yujing Yang: Writing – original draft, Validation, Methodology, Investigation, Formal analysis. **Yong Dong:** Supervision, Resources, Project administration, Methodology, Funding acquisition. **Shichao Liu:** Writing – review & editing, Visualization, Formal analysis. **Shou-gang Duan:** Writing – review & editing, Validation, Methodology, Investigation, Conceptualization. **Chuanqiang Li:** Writing – review & editing, Methodology, Investigation. **Peng Zhang:** Writing – review & editing, Resources, Project administration.

Declaration of Competing Interest

The authors declare that they have no known competing financial interests or personal relationships that could have appeared to influence the work reported in this paper.

Data availability

Data will be made available on request.

Acknowledgments

This research was supported by the National Natural Science Foundation of China (Nos. 51801029) and the Natural Science Foundation of Guangdong Province (No. 2022A1515012591).

References

- [1] J.W. Yeh, S.K. Chen, S.-J. Lin, J.-Y. Gan, T.-S. Chin, T.-T. Shun, C.-H. Tsau, S.-Y. Chang, Nanostructured high-entropy alloys with multiple principal elements: novel alloy design concepts and outcomes, *Adv. Eng. Mater.* 5 (2004) 299–303, <https://doi.org/10.1002/adem.200300567>.
- [2] B. Cantor, I.T.H. Chang, P. Knight, A.J.B. Vincent, Microstructural development in equiatomic multicomponent alloys, *Mater. Sci. Eng. A* 375–377 (2004) 213–218, <https://doi.org/10.1016/j.msea.2003.10.257>.
- [3] Y. Zhang, T.T. Zuo, Z. Tang, M.C. Gao, K.A. Dahmen, P.K. Liaw, Z.P. Lu, Microstructures and properties of high-entropy alloys, *Prog. Mater. Sci.* 61 (2014) 1–93, <https://doi.org/10.1016/j.pmatsci.2013.10.001>.
- [4] F. Otto, A. Dlouhý, C. Somsen, H. Bei, G. Eggeler, E.P. George, The influences of temperature and microstructure on the tensile properties of a CoCrFeMnNi high-entropy alloy, *Acta Mater.* 61 (2013) 5743–5755, <https://doi.org/10.1016/j.actamat.2013.06.018>.
- [5] M. Feuerbacher, T. Lienig, C. Thomas, A single-phase bcc high-entropy alloy in the refractory Zr-Nb-Ti-V-Hf system, *Scr. Mater.* 152 (2018) 40–43, <https://doi.org/10.48550/arXiv.1803.07798>.
- [6] Y.J. Zhao, J.W. Qiao, S.G. Ma, M.C. Gao, H.J. Yang, M.W. Chen, Y. Zhang, A hexagonal close-packed high-entropy alloy: the effect of entropy, *Mater. Des.* 96 (2016) 10–15, <https://doi.org/10.1016/j.matdes.2016.01.149>.
- [7] Y.P. Lu, Y. Dong, S. Guo, L. Jiang, H. Kang, T. Wang, B. Wen, Z. Wang, J. Jie, Z. Cao, H. Ruan, T. Li, A promising new class of high-temperature alloys: eutectic high-entropy alloys, *Sci. Rep.* 4 (2014) 6200, <https://doi.org/10.1038/srep06200>.

- [8] Y. Dong, L. Jiang, Y.P. Lu, T.M. Wang, T.J. Li, Effects of annealing treatment on microstructure and hardness of bulk AlCrFeNiMo_{0.2} eutectic high-entropy alloy, *Mater. Des.* 82 (2015) 91–97, <https://doi.org/10.1016/j.matdes.2015.05.046>.
- [9] T. Wu, L.T. Yu, G. Chen, R.Q. Wang, Y.P. Xue, Y.H. Lu, B.L. Luan, Effects of Mo and Nb on the microstructure and high temperature oxidation behaviors of CoCrFeNi-based high entropy alloys, *J. Mater. Res. Technol.* 27 (2023) 1537–1549, <https://doi.org/10.1016/j.jmrt.2023.10.058>.
- [10] C.H. Tu, Y.C. Lai, S.K. Wu, Y.H. Lin, The Effects of annealing on severely cold-rolled equiatomic HfNbTiZr high entropy alloy, *Mater. Lett.* 5 (2021) 130526, <https://doi.org/10.1016/j.matlet.2021.130526>.
- [11] W. Kai, F.P. Cheng, Y.R. Lin, C.W. Chuang, R.T. Huang, D. Chen, J.J. Kai, C.T. Liu, C.J. Wang, The oxidation behavior of Ni₂FeCoCrAl_x high-entropy alloys in dry air, *J. Alloy. Compd.* 836 (2020) 1–12, <https://doi.org/10.1016/j.jallcom.2020.155518>.
- [12] G. Huang, J. Wu, R. Yuan, Y. Li, F. Meng, P. Lei, C. Lu, F. Cao, Y. Shen, High temperature oxidation behavior and mechanism of Al_{0.3}CuCrFeNi₂ high-entropy alloy with a coherent γ/γ' microstructure, *Corros. Sci.* 195 (2022) 109984, <https://doi.org/10.1016/j.corsci.2021.109984>.
- [13] C.Y. Lu, L.L. Niu, K. Jin, T.N. Yang, P.Y. Xiu, Y.W. Zhang, F. Gao, H.B. Bei, S. Shi, M.R. He, I.M. Robertson, W.J. Weber, L.M. Wang, Enhancing radiation tolerance by controlling defect mobility and migration pathways in multicomponent single-phase alloys, *Nat. Commun.* 7 (2016) 13564, <https://doi.org/10.1038/ncomms13564>.
- [14] Y. Fu, J. Li, H. Luo, X.G. Li, Recent advances on environmental corrosion behavior and mechanism of high-entropy alloys, *J. Mater. Sci. Technol.* 80 (2021) 217–233, <https://doi.org/10.1016/j.jmst.2020.11.044>.
- [15] Q.Y. Zhou, S. Sheikh, P. Ou, D.C. Chen, Q. Hu, S.G. Guo, Corrosion behavior of Hf_{0.5}Nb_{0.5}Ta_{0.5}Ti_{1.5}Zr refractory high-entropy in aqueous chloride solutions, *Electrochim. Commun.* 98 (2019) 63–68, <https://doi.org/10.1016/j.elecom.2018.11.009>.
- [16] X.L. Wan, A.D. Lan, M. Zhang, X. Jin, H.J. Yang, J.W. Qiao, Corrosion and passive behavior of Al_{0.8}CrFeNi_{2.2} eutectic high entropy alloy in different media, *J. Alloy. Compd.* 944 (2023) 169217, <https://doi.org/10.1016/j.jallcom.2023.169217>.
- [17] Y.Z. Shi, B. Yang, X. Xie, J. Brecht, K.A. Dahmen, P.K. Liaw, Corrosion of Al_xCoCrFeNi high-entropy alloys: Al-content and potential scan-rate dependent pitting behavior, *Corros. Sci.* 119 (2017) 33–45, <https://doi.org/10.1016/j.corsci.2017.02.019>.
- [18] X. Duan, T. Han, X. Guan, Y. Wang, H. Su, K. Ming, J. Wang, S. Zheng, Cooperative effect of Cr and Al elements on passivation enhancement of eutectic high-entropy alloy AlCoCrFeNi_{2.1} with precipitates, *J. Mater. Sci. Technol.* 136 (2023) 97–108, <https://doi.org/10.1016/j.jmst.2022.07.023>.
- [19] Liang Wei, Weimin Qin, Corrosion mechanism of eutectic high-entropy alloy induced by micro-galvanic corrosion in sulfuric acid solution, *Corros. Sci.* 206 (2022) 110525, <https://doi.org/10.1016/j.corsci.2022.110525>.
- [20] Z.H. Han, W.N. Ren, J. Yang, A. Tian, Y.Z. Du, G. Liu, R. Wei, G.J. Zhang, Y. Q. Chen, The corrosion behavior of ultra-fine grained CoNiFeCrMn high-entropy alloys, *J. Alloy. Compd.* 816 (2020) 152583, <https://doi.org/10.1016/j.jallcom.2019.152583>.
- [21] W.K. Chai, T. Lu, Y. Pan, Corrosion behaviors of FeCoNiCr_x (x = 0, 0.5, 1.0) multi-principal element alloys: role of Cr-induced segregation, *Intermetallics* 116 (2020) 106654, <https://doi.org/10.1016/j.intermet.2019.106654>.
- [22] X. Huang, Y. Dong, S.M. Lu, C.Q. Li, Z.Q. Zhang, Effects of homogenized treatment on microstructure and mechanical properties of AlCoCrFeNi_{2.2} near-eutectic high-entropy alloy, *Acta Metall. Sin.* 34 (2021) 1079–1086. <http://link.springer.com/journal/40195>.
- [23] H. Wu, J. Xie, H.Y. Yang, L.S. De, C.H. Chen, G.L. Jin, Z.Z. Yi, S.F. Xiao, Comparative study of mechanical and corrosion behaviors of cost-effective AlCrFeNi high entropy alloys, *J. Mater. Eng. Perform.* 31 (2022) 4472–4482, <https://doi.org/10.1007/s11665-021-06563-w>.
- [24] P.J. Shi, Y. Li, Y.B. Wen, Y.Q. Lia, Y. Wang, W.L. Ren, T.X. Zheng, Y.F. Guo, L. Hou, Z. Shen, Y. Jiang, J.C. Peng, P.F. Hu, N.N. Liang, Q.D. Liu, P.K. Liaw, Y.B. Zhong, A precipitate-free AlCoFeNi eutectic high-entropy alloy with strong strain hardening, *J. Mater. Sci. Technol.* 89 (2021) 88–96, <https://doi.org/10.1016/j.jmst.2021.03.005>.
- [25] Y.Z. Shi, L. Collins, R. Feng, C. Zhang, N. Balke, P.K. Liaw, B. Yang, Homogenization of Al_xCoCrFeNi high-entropy alloys with improved corrosion resistance, *Corros. Sci.* 133 (2018) 120–131, <https://doi.org/10.1016/j.corsci.2018.01.030>.
- [26] S. Shuang, Z.Y. Ding, D. Chung, S.Q. Shi, Y. Yang, Corrosion resistant nanostructured eutectic high entropy alloy, *Corros. Sci.* 164 (2020) 108315, <https://doi.org/10.1016/j.corsci.2019.108315>.
- [27] P. Bommersbach, C. Alemany-Dumont, J.P. Millet, B. Normand, Formation and behavior study of an environment-friendly corrosion inhibitor by electrochemical methods, *Electrochim. Acta* 51 (2005) 1076–1084, <https://doi.org/10.1016/j.electacta.2005.06.001>.
- [28] E.E. Oguzie, J.B. Li, Y.Q. Liu, D.M. Chen, Y. Li, K. Yang, F.H. Wang, The effect of Cu addition on the electrochemical corrosion and passivation behavior of stainless steels, *Electrochim. Acta* 55 (2010) 5028–5035, <https://doi.org/10.1016/j.electacta.2010.04.015>.
- [29] J.P. Yuan, Y.J. Yang, S.G. Duan, C.Q. Li, Z.R. Zhang, Rapid design, microstructures, and properties of low-cost Co-free Al-Cr-Fe-Ni eutectic medium entropy alloys, *Mater* 16 (2022) 56, <https://doi.org/10.3390/ma16010056>.
- [30] Z. Wang, J. Jin, G.H. Zhang, X.H. Fan, L. Zhang, Effect of temperature on the passive film structure and corrosion performance of CoCrFeMoNi high-entropy alloy, *Corros. Sci.* 208 (2022) 110661, <https://doi.org/10.1016/j.corsci.2022.110661>.
- [31] H. Feng, J. Dai, H.B. Li, Z.H. Jiang, J.D. Qu, Y. Zhao, S.C. Zhang, T. Zhang, Sn microalloying enhances corrosion resistance of stainless steel by accelerating heterogeneous nucleation of passive film, *Corros. Sci.* 201 (2022) 110279, <https://doi.org/10.1016/j.corsci.2022.110279>.
- [32] B. Hirschorn, M. Orazem, B. Tribollet, V. Vivier, Is Frateur, M. Musiani, Determination of effective capacitance and film thickness from constant-phase-element parameters, *Electrochim. Acta* 55–56 (2010) 6218–6227, <https://doi.org/10.1016/j.electacta.2009.10.065>.
- [33] M.E. Orazem, I. Frateur, B. Tribollet, V. Vivier, S. Marcellin, N. Péb're, A.L. Bunge, E.A. White, D.P. Riemer, M. Musiani, Dielectric properties of materials showing constant-phase-element (CPE) impedance response, *J. Electrochim. Soc.* 160 (2013) C215, <https://doi.org/10.1149/2.033306jes>.
- [34] S. Shuang, Q. Yu, X. Gao, Q.F. He, J.Y. Zhang, S.Q. Shi, Y. Yang, Tuning the microstructure for superb corrosion resistance in eutectic high entropy alloy, *J. Mater. Sci. Technol.* 109 (2022) 197–208, <https://doi.org/10.1016/j.jmst.2022.08.069>.
- [35] S. Marcellin, N. Péb're, S. Régnier, Electrochemical characterisation of a martensitic stainless steel in a neutral chloride solution, *Electrochim. Acta* 87 (2013) 32–40, <https://doi.org/10.1016/j.electacta.2012.09.011>.
- [36] J. Yao, D.D. Macdonald, C. Dong, Passive film on 2205 duplex stainless steel studied by photo-electrochemistry and ARXPS methods, *Corros. Sci.* 146 (2019) 221–232, <https://doi.org/10.1016/j.corsci.2018.10.020>.
- [37] E.J. Liu, X. Chen, Z.M. Pan, J. Xu, Y.B. Chen, D.B. Shan, B. Guo, Enhanced corrosion performance of S136 steel after nanosecond pulsed laser polishing, *J. Mater. Res. Technol.* 20 (2022) 1328–1340, <https://doi.org/10.1016/j.jmst.2022.07.132>.
- [38] K. Morshed-Behbani, P. Najafisayar, M. Pakshir, M. Shahsavari, An electrochemical study on the effect of stabilization and sensitizing heat treatments on the intergranular corrosion behaviour of AISI 321H austenitic stainless steel, *Corros. Sci.* 138 (2018) 28–41, <https://doi.org/10.1016/j.corsci.2018.03.043>.
- [39] Z.C. Zhang, A.D. Lan, M. Zhang, J.W. Qiao, Effect of Ce on the pitting corrosion resistance of non-equiatomic high-entropy alloy Fe₄₀Mn₂₀Cr₂₀Ni₂₀ in 3.5 wt% NaCl solution, *J. Alloy. Compd.* 909 (2022) 164641, <https://doi.org/10.1016/j.jallcom.2022.164641>.
- [40] A. Fattah-Alhosseini, M. Golozar, A. Saatchi, K. Raeissi, Effect of solution concentration on semiconducting properties of passive films formed on austenitic stainless steels, *Corros. Sci.* 52 (2010) 205–209, <https://doi.org/10.1016/j.corsci.2009.09.003>.
- [41] J.W. Diggle, T.C. Downie, C. Goulding, Anodic oxide films on aluminum, *Chem. Rev.* 69 (1969) 365–405.
- [42] W. Chen, R. Zhou, W. Li, Y.H. Chen, T.H. Chou, X. Wang, Y. Liu, Y. Zhu, J. Huang, Effect of interstitial carbon and nitrogen on corrosion of FeCoCrNi multi-principal element alloys made by selective laser melting, *J. Mater. Sci. Technol.* 148 (2023) 52–63, <https://doi.org/10.1016/j.jmst.2022.10.027>.
- [43] H. Luo, Z. Li, A.M. Mingers, D. Raabe, Corrosion behavior of an equiatomic CoCrFeMnNi high-entropy alloy compared with 304 stainless steel in sulfuric acid solution, *Corros. Sci.* 134 (2018) 131–139, <https://doi.org/10.1016/j.corsci.2018.02.031>.
- [44] A. Foelske, H. Strehblow, Passivity of cobalt in borate buffer at pH 9.3 studied by X-ray photoelectron spectroscopy, *Surf. Interface Anal.* 29 (2000) 548–555, [https://doi.org/10.1002/1096-9918\(200008\)29:8<548::AID-SIA902>3.0.CO;2-Q](https://doi.org/10.1002/1096-9918(200008)29:8<548::AID-SIA902>3.0.CO;2-Q).
- [45] T. Nishimura, H. Katayama, K. Noda, T. Kodama, Effect of Co and Ni on the corrosion behavior of low alloy steels in wet/dry environments, *Corros. Sci.* 42 (2000) 1611–1621, [https://doi.org/10.1016/S0010-938X\(00\)00018-4](https://doi.org/10.1016/S0010-938X(00)00018-4).
- [46] C. Delgado-Alvarado, P.A. Sundaram, A study of the corrosion behavior of gamma titanium aluminide in 3.5 wt% NaCl solution and seawater, *Corros. Sci.* 49 (2007) 3732–3741, <https://doi.org/10.1016/j.corsci.2007.04.001>.
- [47] H. Ezuber, A. El-Houd, F. El-Shawesh, A study on the corrosion behavior of aluminum alloys in seawater, *Mater. Des.* 29 (2008) 801–805, <https://doi.org/10.1016/j.matedes.2007.01.021>.
- [48] Y.Q. Wang, N. Li, B. Yang, Effect of ferrite on pitting corrosion of Fe₂₀Cr₁₀Ni cast austenite stainless steel for nuclear power plant pipe, *Corros. Eng. Sci. Technol.* 50 (2015) 330–337, <https://doi.org/10.1179/1743278214Y.0000000229>.
- [49] P.P. Sarkar, P. Kumar, M.K. Manna, P.C. Chakraborti, Microstructural influence on the electrochemical corrosion behaviour of dual-phase steels in 3.5% NaCl solution, *Mater. Lett.* 59 (2005) 2488–2491, <https://doi.org/10.1016/j.mattlet.2005.03.030>.
- [50] L.F. Song, W.B. Hu, B.K. Liao, S. Wan, L. Kang, X.P. Guo, Corrosion behavior of Al_{0.2}Cr_{0.2}FeNi_{2.1} eutectic high-entropy alloy in Cl⁻ containing solution, *J. Alloy. Compd.* 938 (2023) 168609, <https://doi.org/10.1016/j.jallcom.2022.168609>.
- [51] H. Luo, H. Su, C. Dong, X. Li, Passivation and electrochemical behavior of 316L stainless steel in chlorinated simulated concrete pore solution, *Appl. Surf. Sci.* 400 (2017) 38–48, <https://doi.org/10.1016/j.apsusc.2016.12.180>.
- [52] Y. Wang, S. Jiang, Y. Zheng, W. Ke, W. Sun, J. Wang, Effect of porosity sealing treatments on the corrosion resistance of high-velocity oxy-fuel (HVOF)-sprayed Fe-based amorphous metallic coatings, *Surf. Coat. Technol.* 206 (2011) 1307–1318, <https://doi.org/10.1016/j.surfcoat.2011.08.045>.
- [53] Z.J. Shi, Z.B. Wang, X.D. Wang, S. Zhang, Y.G. Zheng, Effect of thermally induced B2 phase on the corrosion behavior of an Al_{0.3}CoCrFeNi high entropy alloy, *J. Alloy. Compd.* 903 (2022) 163886, <https://doi.org/10.1016/j.jallcom.2022.163886>.
- [54] Y.Z. Shi, L. Collins, N. Balke, P.K. Liaw, B. Yang, In-situ electrochemical-AFM study of localized corrosion of Al_xCoCrFeNi high-entropy alloys in chloride solution, *Appl. Surf. Sci.* 439 (2018) 533–544, <https://doi.org/10.1016/j.apsusc.2018.01.047>.